Experimental measurements and theoretical modeling of high-pressure mass densities and interfacial tensions of carbon dioxide + n-heptane + toluene and its carbon dioxide binary systems

Constanza Cumicheo [a,b], Marcela Cartes [a], Erich A. Müller [b], Andrés Mejía[*, a]

[a] Departamento de Ingeniería Química, Universidad de Concepción POB 160 – C, Correo 3, Concepción, Chile.

[b] Department of Chemical Engineering, Imperial College London, South Kensington Campus, London SW7 2AZ, U. K.

ABSTRACT

Experimental determination and theoretical predictions of the isothermal (344.15 K) mass densities and interfacial tensions for the system carbon dioxide (CO2) with heptol (n-heptane + toluene) mixtures varying liquid volume fraction compositions of toluene (0, 25, 50, 75, 100 % v/v) and over the pressure range 0.1 to 8 MPa are reported. Measurements are carried out on a high-pressure device that includes a vibrating tube densimeter and a pendant drop tensiometer. Theoretical modeling of mass densities phase equilibria and interfacial properties (i.e., interfacial tension and interfacial concentration profiles) are performed by employing the Square Gradient Theory using an extension of the Statistical Associating Fluid Theory equation of state that accounts for ring fluids. The experimental bulk phase equilibrium densities and interfacial tensions obtained are in very good agreement with the theoretical predictions. Although there are no previous experimental data of these mixtures at the conditions explored herein, the results follow the same trends observed from experimental data at other conditions. The combination of experimental and modeling approaches provides a route to simultaneously predict phase equilibrium and interfacial properties within acceptable statistical deviations.

For the systems and conditions studied here, we observe that the phase equilibrium of the mixtures display zeotropic vapor-liquid equilibria with positive deviations from ideal behavior. The mass bulk densities behave ordinarily whereas the interfacial tensions decrease as the pressure or liquid mole fraction of CO2 increases and/or the ratio toluene/heptane decreases. The interfacial concentration along the interfacial region exhibits a remarkable high excess adsorption of CO2, which increases with pressure and it is larger in n-heptane than in toluene. Toluene does not exhibit any special adsorption activity

[*] To whom correspondence should be addressed. e_mail: amejia@udec.cl

whereas n-heptane displays surface activity only at low pressure in a very narrow range for the case of CO2 + (25% n-heptane + 75% toluene) mixture.

Keywords: High-pressure interfacial tension; high-pressure density; CO2 + hydrocarbon mixtures; Square gradient theory; SAFT-VR-Mie EoS; EOR

1. Introduction

Enhanced Oil Recovery (EOR) refers to the procedures and processes put in place to raise the efficiency of oil recovery from existing hydrocarbon reservoirs fields. In a traditional EOR, a pressurized miscible gas fluid (*e.g.*, CO_2) is injected into the reservoir to aid in the displacement of the remaining crude oil in the well. This miscible displacement process maintains reservoir pressure and improves the oil displacement playing on the decrease in the interfacial tension (IFT) between oil and water. In this tertiary stage, approximately, from 30 % to 60 % of the original oil may be extracted. In order to control and to obtain an efficient recovery in EOR, it is necessary to know the IFT of mixtures composed of the miscible gas fluid, water, paraffinic hydrocarbons (from methane to triacontane or larger) and aromatic hydrocarbons (*e.g.*, benzene, pyridine, toluene, etc.). IFT allows establishing the minimum miscibility pressure, below which the gas flood becomes immiscible and EOR becomes inefficient (see Refs. [1,2,3,4] and references therein). In addition, the magnitude of IFT controls the wetting behavior between fluid – fluid and fluid – solid phases (*i.e.*, distribution of gas, oil, and water in the reservoir) [5,6,7]. The knowledge of IFT between CO_2, hydrocarbons (paraffinic and aromatic), and water are not only needed for the understanding, improvement and optimization of oil recovery by EOR processes, but also to control other physicochemical problems associated to oil extraction such as asphaltene precipitation. In fact, the dramatic change of the slope of IFT – pressure provides a route to find the onset pressure at which asphaltene precipitation occurs [4,8]. In addition to miscibility issues, EOR in hydrocarbon reservoirs takes place at extreme thermodynamic conditions ($T > 310$ K and $P > 8$ MPa) [9,10,11], where CO_2 + hydrocarbon mixtures exhibit complex multiphase equilibria (see for instances Refs. [12,13,14]) affecting the interfacial properties.

Because of the extreme T and P conditions and the complex behavior of phase equilibria, recent works on interfacial properties of CO_2 + hydrocarbon mixtures involved in EOR extraction have been carried out by using complementary techniques, where experimental determinations, theoretical approaches and molecular simulations are the most common approaches. From an experimental point of view, IFT of these mixtures has been measured by using pendant drop tensiometry (see for instance Refs. [15,16,17] and references therein). On the other hand, theoretical descriptions of these mixtures have been made by employing Density Functional Theory (see for example Refs. [18,19]) and more popularly the Square Gradient Theory (SGT) (see for instances Refs. [16,17,20,21,22,23,24,25,26,27,28]). Furthermore, molecular simulations based either on Molecular Dynamics or Monte Carlo schemes have also been employed [16,29,30]. As it was previously showed (see for instances Refs. [16,17,29]), a complete description of bulk phase and interfacial properties, including IFT, are obtained when experimental

determinations are combined with theoretical models and/or molecular simulations. This interrelated combination provides a route to extrapolate the experimental data to extreme conditions, exploring unmeasurable quantities such as interfacial concentration along the interfacial region, surface activity, etc. or to validate theories and the force fields used in molecular simulations.

As part of our ongoing research work, which is devoted to the description of interfacial properties for CO_2 + n-alkanes mixtures [16,17,20,21,22,29], this work is focused on the experimental determination and theoretical modeling of bulk phase equilibrium densities and interfacial tensions of the CO_2 + {n-heptane (n-C_7H_{16}) + toluene (C_7H_8)} or CO_2 + *heptol* mixtures with different liquid volume fraction compositions of toluene (0, 25, 50, 75, 100 %*v/v*) at 344.15 K and over the pressure range 0.1 to 8 MPa. Measurements are carried out on a high-pressure device that includes a vibrating tube densimeter and a pendant drop tensiometer. Theoretical modeling of mass densities phase equilibria and interfacial properties, including interfacial tension and interfacial concentration profiles, are calculated by employing the van der Waals Square Gradient Theory (SGT) using a new extension of the Statistical Associating Fluid Theory (SAFT VR Mie) [31] equation of state (EoS) that includes an extra term that accounts not only for monomer-like fluid (CO_2), chain-like fluid (n-C_7H_{16}) but also for ring-like fluids (C_7H_8). [32]

1.1 Reported values

Recently, Al Ghafri et al. [33] reported experimental data and theoretical modeling for the phase equilibria for the CO_2 + n-C_7H_{16} + C_7H_8 ternary system. The experimental conditions cover the temperature range from 298 K to 423 K at pressures up to 16 MPa, whereas the theoretical modeling was carried out by using the Statistical Associating Fluid Theory (SAFT) based on Mie potentials where the involved molecular parameters were obtained from the group-contribution approach [34]. In addition to the ternary system, Al Ghafri et al. [33] present an abridged review of both experimental data and theoretical modeling for two of the constituent binaries: CO_2 + C_7H_8 and CO_2 + n-C_7H_{16}.

According to DECHEMA [35] the bulk densities (liquid and vapor) of the CO_2 binary mixtures have been measured in a broad range of temperatures and pressure. Specifically, for the case of CO_2 + n-C_7H_{16} mixture, the bulk liquid densities have been reported at three mole fractions of liquid CO_2 (x_{CO2} = 0.2918; 0.3888; 0.4227) from 316.28 K to 459.37 K, and over the pressure range of 4.5 to 55.5 MPa by Fenghour et al. [36]. Medina-Bermúdez et al. [37] reported additional values of liquid density at five mole fractions of liquid CO_2 (x_{CO2} = 0.0218, 0.3148, 0.5085, 0.7514, 0.9496) at the temperature range 313 K to 363 K, and over the pressure range (2 to 25) MPa. For the vapor phase, Zhang et al. [38] reported bulk densities at 308.15 K and over the pressure range from (5.94 to 10.19) MPa and Kalra et al. [39] reported the

density at the following conditions: 310.29 K over (0.18 to 7.56) MPa; 352.29 K over (0.42 to 11.61) MPa and at 394.26 K over (1.13 to 13.3) MPa. For the case of CO_2 + C_7H_8 several authors have been reported bulk densities at different isothermal conditions at pressures up to 15 MPa. Specifically, Park et al. [40] have been reported the density for both liquid and gas phase at the following conditions: 333.2 K and (4.45 to 9.797) MPa; 363.2 K and (3.975 to 13.3) MPa and 393.2 K and (6.438 to 15.35) MPa. The density of liquid phase has been reported by Poehler and Kiran [41] at the isothermal range (323 to 423) K and in a broad pressure range (9.85 to 65.07) MPa, and Zirrahi et al. [42] have also reported the liquid density at the isothermal conditions: (298.15; 308.15; 338.15; 363.15) K and over the pressure range (0.88 to 5) MPa. Other intermediate conditions have been reported by Wu et al. [43] (323 to 398) K and (7.86 to 64.76) MPa. For the vapor phase, Senger et al. [44] have reported experimental data at 310 K, 313 K, 333 K and over (8.5 to 13.5) MPa.

In terms of IFT, a search of the DECHEMA [35] and Landolt-Börnstein data bases [45] reveals that the CO_2 + n-C_7H_{16} binary mixture is the only mixture where interfacial tensions have been previously reported. Specifically, Niño Amézquita et al., [46], Jaeger et al., [47] and Zolghadr et al., [48] reported interfacial tension as a function of temperature and pressure that cover the temperature and pressure ranges from 313.15 to 393.15 K and from 0.1 to 11.2 MPa, respectively. From a theoretical view, Niño Amézquita et al., [46] modeled both phase equilibria and interfacial properties (*i.e.*, interfacial profiles along the interfacial region, interfacial thickness, interfacial tension) using the PCP-SAFT-EoS in combination with SGT. According to the presented results, the predictions from theory display very good agreement to the reported experimental data.

This paper is organized as follows: we first describe the experimental equipment and measurement details (Section 2). We then summarize the main expressions of the SAFT-VR-Mie EoS model and the square gradient theory (Section 3). Following, we present and discuss the main results of bulk phase equilibrium densities (vapor and liquid), the interfacial tensions and the interfacial concentration profiles and the surface activity in Section 4. Finally, we summarize the main conclusions of this work in Section 5.

2. Experimental Section

2.1 Purity of Materials.

Carbon dioxide was purchased from Linde S.A. (Chile) with a certified purity greater than 99.9 %, whereas n-heptane and toluene were purchased from Merck and used without further purification. Table 1 reports the purity of the components (as determined by gas chromatography, GC), together with the

mass densities ($\hat{\rho}$), and the interfacial tensions (γ) of pure fluids at 344.15 K and atmospheric pressure. The experimental values are also compared with those previously reported by NIST – REFPROP [49].

2.2 Apparatus and procedure

2.2.1. Density measurements

The mass density ($\hat{\rho}$) of pure fluids is measured at 344.15 K and atmospheric pressure using a DMA 5000 densimeter (Anton Paar, Austria). For the case of mixtures CO_2 + {(1-v) n-C_7H_{16} + v C_7H_8}, with v = (0, 0.25, 0.50, 0.75, 1), at 344.15 K and at pressures over the atmospheric pressure, $\hat{\rho}$ in the liquid and the vapor phases are measured at the experimental temperature and pressure using a DMA HP densimeter (Anton Paar GmbH, Austria). In both cases (atmospheric and high pressure) the mass density is measured with an accuracy of 5×10^{-3} kg m^{-3}.

In both densimeters, the mass density determination is based on measuring the period of oscillation of a vibrating U-shaped tube filled with the fluid mixture sample. During the operation, the temperature of the apparatus is maintained constant to within ± 0.01 K. Pressure, in turn, is measured by means a Swagelok type S pressure transducer connected to the densimeter, and maintained constant to within ± 0.001 kPa by means of the high-pressure syringe pump (Teledyne Isco Pump. Model 100DM, USA). The density measurements are repeated 25 times for each condition and averaged accordingly.

2.2.2. Interfacial Tension Cell.

A pendant drop tensiometer model IFT-10, manufactured by Temco Inc. (USA) is used for interfacial tension measurements. The pendant drop cell is a stainless steel cylindrical chamber (with an inner volume of ~ 42 cm^3), with two injection orifices one at the top and the other at the bottom of the chamber. On the top orifice, a stainless-steel needle (1.4 mm i.d. and 2.45 mm o.d.) is placed for generating pendant drops. The bottom orifice is connected to the high-pressure syringe pump (Teledyne Isco Pump. Model 100DM, USA), which is used to compress CO_2 from a commercial ultra-high purity CO_2 cylinder and maintained the experimental pressure constant within ± 0.001 kPa.

The chamber is equipped with appropriately sealed borosilicate glass windows, which allows visualization of the inner space during operation. The light beam source, located at one side of the visualization axis, is a led fiber optic light source (20W LED Fiber Optic, AmScope, USA) covered by

a white diffuser made of Teflon. The camera, located at opposite side of the visualization axis, is a monochrome video camera model CS8320Bi (Toshiba Teli, Corp., Japan) connected to a personal computer through a frame grabber card. The temperature of the cell is measured by means a K-type thermocouple, and maintained constant to within ± 0.1 K by means of electric band heaters operated by a Watlow temperature controller model TC-211-K-989 (USA). The tensiometer, the light source and the camera are mounted on a free vibration table (Vibraplane, model 2210, USA) in order to avoid the effect of noisy measurements due to external vibrations. Interfacial tension measurements were made by analyzing images of liquid (n-heptane and toluene) pendant drops generated at the tip of an injection needle, which is surrounded by CO_2, by using the DROPimage Advanced software version 1.5 (Ramé – Hart instruments, co. USA). [50]

The experimental procedure for determining interfacial tension is as follows. The cell is heated to the desired experimental temperature (344.15 K), and then it is slightly pressurized with CO_2. After degasification in an ultrasonic bath, the fluids (n-heptane and toluene) are mixed in a volume proportion from 0 to 100 % of toluene. This liquid mixture is pumped through a stainless-steel tube to the needle tip. The pump is a positive displacement ELDEX HP Series Model B-100-S-2 CE (USA). Initially, a small portion of the liquid mixture is pumped into the chamber in order to saturate the gas that fills the cell. Then, the cell is pressurized to the desired experimental pressure and a liquid drop is generated at the tip of the needle. The pressure in the IFT cell is maintained constant to within ± 0.10 kPa by means of the high-pressure syringe pump.

Once the drop is formed and the desired experimental temperature and pressure are reached, it is necessary to wait, approximately, 5 to 10 minutes until the drop reaches an equilibrium state. This value is based on the experimental evidence of the time evolution of interfacial tension. After this equilibration step, the drop dimensions are recorded (at least during 6 hours) in order to check the stability of its geometry.

Once the shape and volume of the drop are deemed constant, the equatorial diameter of the drop, d_e (the largest one), and the horizontal diameter of the drop, d_s, which is located at a distance d_e from the apex of the drop are recorded and, simultaneously, the liquid and the gas phases are transported to the high-pressure densimeter, through a heated stainless steel tube, in order to measure the mass density of the liquid mixture (*heptol*) saturated with CO_2 ($\hat{\rho}_L$) and the mass density of CO_2 saturated with *heptol* ($\hat{\rho}_G$) both densities are measured at the experimental temperature and pressure.

Based on the experimental measurements of d_e, d_s, $\hat{\rho}_L$ and $\hat{\rho}_G$, the interfacial tension, γ, is obtained through the following expression:

$$\gamma = (\hat{\rho}_L - \hat{\rho}_G)\, g d_e^2 f\,(d_e, d_s) \tag{1}$$

where g is the local gravitational constant (9.81 m•s^{-2}), and $f(d_s,d_e)$ corresponds to a function related to the silhouette of the drop, whose value is determined from numerical tables.[51] In this work, γ and $\hat{\rho}$ are measured at a constant temperature of 344.15 K and over the pressure range 0.1 MPa to 8 MPa.

In a pendant drop tensiometer the tension γ is not measured directly; therefore, one must note that the uncertainties of γ values are affected by the value of temperature, pressure, density difference, the experimental reproducibility of γ itself and its standard uncertainties. In order to quantify these effects in the expanded or combined relative uncertainty of γ, u_c, the following relationship [52] has been considered:

$$u_c^2(\gamma) = \left[\frac{1}{\gamma}\left(\frac{\partial \gamma}{\partial P}\right)_T \delta P\right]^2 + \left[\frac{\delta \Delta\rho}{\Delta\rho}\right]^2 + \left[\frac{\sigma(\gamma)}{\gamma}\right]^2 \tag{2}$$

In Eq. (2) δp and $\delta \Delta\rho$ correspond to the standard uncertainties in pressure and density, respectively. $\sigma(\gamma)$ is the standard deviation of γ which, together with the maximum value of partial derivatives of γ in P, have directly been estimated from experimental data. For the binary and ternary systems investigated here, the average u_c, value was found to be 0.73 %. Therefore, the expanded relative uncertainty of γ at 95 % confidence was 1.3 %.

In addition to the uncertainty associated to γ, (u_c), the dimensionless Worthing number (Wo) is used to evaluate the interfacial tension accuracy. Wo is defined as [53]:

$$Wo = \frac{(\hat{\rho}_L - \hat{\rho}_G)\, g V_d}{\pi \gamma d_n} \tag{3}$$

In Eq. (3) $\hat{\rho}_L$, $\hat{\rho}_G$, g and γ are defined in Eq. (1), whereas V_d is the drop volume d_n is the needle internal diameter (≈ 1.4 mm). According to Berry et al. [53], $Wo \approx 0.5$ to 1 implies an accurate value γ and $Wo << 1$ is associated to inaccurate value of γ. In this work, for CO_2 + {(1-v) n-C_7H_{16} + v C_7H_8} with v = (0, 0.25, 0.50, 0.75, 1) at 344.15 K and 0.1 to 8 MPa, the average of this number was $Wo \approx 0.7$.

Finally, it is important to recall that the chamber cleaning plays a key role in the accuracy of the pendant drop technique, since negligible impurity concentrations strongly affect γ measurements. Consequently,

appropriate precautions were taken when cleaning the chamber surfaces by replicating experimental γ values of the pure fluids at 344.15 K and 0.1 MPa (see Table 1).

For additional details concerning to the pendant drop technique and implementation, the reader is redirected to the references: Andreas et al. [51], Rusanov and Prokhorov [54], Ambwani and Fort [55] and Evans [56].

3. Theoretical Section

3.1 The Statistical Associating Fluid Theory (SAFT) Model

For modeling the bulk phase equilibria and their bulk densities, we employ here an extension of the SAFT VR Mie EoS [31] which aims at accurately modeling both chain-like and planar ring-like non-associating fluids. [32]. In this version, the molecules are conformed of segments interacting through the Mie potential, ϕ^{Mie}: [57]

$$\phi^{Mie}(r_{ij}) = C\varepsilon\left[\left(\frac{\sigma}{r_{ij}}\right)^{\lambda_r} - \left(\frac{\sigma}{r_{ij}}\right)^{\lambda_a}\right] \tag{4}$$

In Eq. (4) λ_r and λ_a are the repulsion and attraction parameters of the intermolecular potential, respectively, r_{ij} is the center-to-center distance of the interacting segments, ε is the energy scale corresponding to the potential well depth, σ length scale, corresponding loosely with an effective segment diameter, and C is a constant defined as:

$$C = \frac{\lambda_r}{\lambda_r - \lambda_a}\left(\frac{\lambda_r}{\lambda_a}\right)^{\frac{\lambda_a}{\lambda_r - \lambda_a}} \tag{5}$$

The corresponding expression of Helmholtz energy density of this SAFT EoS for non-associating chain-ring fluid is given by [31,32]

$$a = \left(a^{IG} + a^{MONO} + a^{CHARI}\right)\rho\frac{N_{av}}{\beta} \tag{6}$$

where $a = A / (N k_B T)$, A being the total Helmholtz energy, N the total number of molecules, N_{av} the Avogadro constant, T the temperature, k_B the Boltzmann constant, $\beta = 1/ (k_B T)$, and ρ the molar density of the mixture. In Eq. (6), a^{IG} is the ideal gas reference, a^{MONO} represents monomer (unbounded) contribution, while a^{CHARI} accounts for the formation of chain and ring molecules. The corresponding expression for each contribution are summarized in the following expressions (see Refs. [31,32]):

$$a^{IG} = \left[\sum_{i=1}^{n_c} x_i ln\left(x_i \rho N_{av} \Lambda^3\right)\right] - 1 \tag{7.a}$$

$$a^{MONO} = \left(\sum_{i=1}^{n_c} x_i m_{si}\right)\left(a^{hs} + \beta a_1 + \beta^2 a_2 + \beta^3 a_3\right) \tag{7.b}$$

$$a^{CHARI} = -\sum_{i=1}^{n_c} x_i \left(m_{si} - 1 + \chi_i \eta_i\right) ln\left[g_{ii}^{Mie}(\sigma)\right] \tag{7.c}$$

where x_i is the mole fraction of fluid i; Λ is the thermal de Broglie's wavelength; n_c is the number of components in the mixture. m_{si} is the number of spherical segments making up the chains or rings of component i. a^{hs} is the Helmholtz energy density of the Carnahan and Starling hard sphere; a_1, a_2, a_3 are the first-, second-, and third-order perturbation terms of hard sphere; $g_{ii}^{Mie}(\sigma)$ is radial distribution function of the Mie potential. χ_i is defined as a parameter for fluid i, which is a function of m_{si} and the actual geometrical connection of the ring. η_i is the packing fraction of fluid i, defined as [31]:

$$\eta_i = m_{si} \pi N_{av} x_i \rho d_i^3 / 6 \tag{8}$$

where d_i is the hard-sphere diameter of fluid i, which is defined by the following integral expression:

$$d_i = \int_0^{\sigma_i} \left(1 - exp\left(-\beta \phi_i^{Mie}(r)\right)\right) dr \tag{9}$$

Specific details concerning the terms in Eqs. (6) to (9) are extensively described in Refs. [31,32].

From the previous expressions, it is possible to state that pure components are characterized by six parameters: m_s, λ_r , λ_a, ε, σ and χ. However, this number can be reduced through the following physical arguments:

a. Considering the conformality of the Mie potentials [58,59], one can recognize that infinite pairs of exponents (λ_r - λ_a) will reproduce the same macroscopic fluid properties, as long as the selected pair gives the same value of the van der Waals constant, α, which is defined as: [60]

$$\alpha = \frac{1}{\varepsilon\sigma^3}\int_{\sigma}^{\infty}\phi^{Mie}(r)\,r^2 dr = C\left[\left(\frac{1}{\lambda_a - 3}\right) - \left(\frac{1}{\lambda_r - 3}\right)\right] \tag{10}$$

On the basis of Eq. (10), it is possible to fix one of the exponents in the Mie potential without a loss of generality. Following the London dispersion theory [61], a value of $\lambda_a = 6$ (or $\lambda_a = 6.66$ for the case of CO_2 where a quadrupole moment affect the dispersion) is taken as a fixed value, leaving $\lambda = \lambda_r$, as the only adjustable parameter.

b. The molecules that conform the pure fluids can be represented as coarse-grained (CG) beads. These CG beads corresponding to "super"-united-atoms. In this work, we modeled CO_2 as a single sphere ($m_{s1} = 1$); n-C_7H_{16} is formed by two tangential spheres ($m_{s2} = 2$); whereas C_7H_8 is represented by an equilateral triangle of three spheres ($m_{s3} = 3$).

c. Based on the value of m_{si} and the geometrical connection of the beads, $\chi = 0$ for CO_2 and n-C_7H_{16} whereas $\chi = 1.4938$ for C_7H_8.

Considering the above simplifications, pure components are now characterized by three parameters: λ, ε, and σ. As we demonstrated in a previous works, [32,58,62] these molecular parameters can be found by invoking a three parameter corresponding states principle. In the latter approach, the critical temperature (T_c), the acentric factor (ω) and the liquid density at a reference temperature (ρ_{ref}) of the fluid are used to calculate λ, ε, and σ. In this work, we use this methodology to calculate the molecular parameters of n-C_7H_{16} and C_7H_8. This procedure can be also used for CO_2, but we use here the molecular parameters reported by Avendaño et al [63]. These parameters have been used to describe our previous works relate to CO_2 + n-alkanes [16,17]. Table 2 summarizes the SAFT parameters for pure fluids as used in this work.

The SAFT EoS is extended to mixtures by using unlike parameters which are defined by applying combination rules [31]. The unlike size parameter, σ_{ij} is obtained using an arithmetic mean:

$$\sigma_{ij} = \frac{\sigma_{ii} + \sigma_{jj}}{2} \tag{11}$$

while the unlike Mie attractive interaction energy (or cross potential well depth), ε_{ij} is obtained using a Berthelot-like geometric average:

$$\varepsilon_{ij} = \left(1 - k_{ij}\right) \frac{\sqrt{\sigma_{ii}^3 \sigma_{jj}^3}}{\sigma_{ij}^3} \sqrt{\varepsilon_{ii} \varepsilon_{jj}} \tag{12}$$

where k_{ij} is a binary interaction parameter, which can be obtained from experimental data of phase equilibria. The cross attractive and repulsive exponents involved in the Mie potential are calculated as:

$$(\lambda_{ij} - 3) = \sqrt{(\lambda_{ii} - 3)(\lambda_{jj} - 3)} \tag{13}$$

where the same functional form applies to both the repulsion and attraction parameters of the intermolecular potential.

At this point, it is worthy to comment on the predictive capability and transferability of the SAFT approach. On the one hand, the parameters for pure fluids can be directly obtained from three very common physical properties (T_c, ω, ρ_{ref}). For the mixtures, there are only an extra parameter for binary interactions, k_{ij}. This value is usually small due to the size and energy caused by mixing mixtures are absorbed by the second and third terms in Eq. (12). k_{ij} is fixed for the case of binary mixtures by using VLE data, therefore for ternary or multicomponent mixtures, the SAFT extended to mixtures is fully predictive. On the other hand, the molecular parameters that describe pure fluid and fluid mixtures can be directly transferred to carry out molecular simulations without any extra modification. For specific details for this top-down approach to parametrize force field in molecular simulations the reader is redirected to Müller and Jackson's review. [64]

The isothermal bulk phase equilibrium is calculated from the SAFT EoS model by using the following equations:

$$\left[\rho^2 \frac{\partial}{\partial \rho}\left(\frac{a}{\rho}\right)_{T,N}\right]^V = \left[\rho^2 \frac{\partial}{\partial \rho}\left(\frac{a}{\rho}\right)_{T,N}\right]^L \Rightarrow P^V = P^L = P^0 \tag{14.a}$$

$$\left(\frac{\partial a}{\partial \rho_i}\right)^{L}_{T,V,\rho_{j\neq i}} = \left(\frac{\partial a}{\partial \rho_i}\right)^{V}_{T,V,\rho_{j\neq i}} \Rightarrow \mu_i^L = \mu_i^V = \mu_i^0 \qquad i = 1, \ldots, n_c \qquad (14.b)$$

$$\left(\frac{\partial^2 a}{\partial \rho_i^2}\right)^{0}_{T^0,V^0,\rho^0_{j\neq i}} = \left(\frac{\partial \mu_i}{\partial \rho_i}\right)^{0}_{T^0,V^0,\rho^0_{j\neq i}} > 0 \qquad i = 1, \ldots, n_c \qquad (14.c)$$

where μ_i is the chemical potential of species *i* and *P* is the pressure. The superscript *0* denotes that these variables are evaluated at the phase equilibrium condition of the bulk phases (*V*, *L*). Eqs. (14.a) to (14.c) are equivalent to the necessary conditions of phase equilibrium for bulk phases. Specifically, Eq. (14.a) corresponds to the mechanical equilibrium condition while Eq. (14.b) expresses the chemical potential constraint. Eq. (14.c) is a differential stability condition for interfaces, comparable to the Gibbs energy stability constraint of a single phase. [65]

In order to provide for a complete theoretical model to describe the experimental determinations reported in this work (*i.e.*, bulk phase equilibrium densities and interfacial tensions), the corresponding k_{ij} values have been regressed from *P – x,y* experimental data at 344.15 K or at a closer isothermal condition (see Refs. [66,67,68,69]). Table 3 summarizes the optimal values of k_{ij}, the temperature condition of the fitting, the absolute average deviation in pressure and the absolute deviation in vapor mole fraction.

3.2. Square Gradient Theory for modeling interfacial behavior

Interfacial properties such as interfacial density profiles and interfacial tensions for pure fluids and fluid mixtures can be calculated by applying the van der Waals square gradient theory (SGT) to an accurate EoS model, such as the EoS used here: SAFT VR Mie EoS [31,32]

Within the SGT, the interfacial tension of a mixture, γ, is given by the following integral expression: [70,71,72]

$$\gamma = \sqrt{2}\int_{\rho_s^V}^{\rho_s^L} \sqrt{\Delta\Omega\left[\sum_{i,j=1}^{n_c}\sqrt{c_i c_j}\left(\frac{d\rho_i}{d\rho_s}\right)\left(\frac{d\rho_j}{d\rho_s}\right)\right]}\, d\rho_s \qquad (15)$$

In Eq. (15), c_i is the influence parameter of species *i*. ρ_s^V and ρ_s^L corresponds to the molar concentration of component *s* at the bulk vapor (*V*) and liquid (*L*) phases, respectively. ρ_k is the interfacial molar concentration for species (*k* = *i*,*j* or *s*). The lower script *s* represents the component (*i* or *j*), whose pattern, along the interface region, shows a monotonic behavior. This selection is based on the physical fact that

the less volatile component should not accumulate in the interfacial region and, therefore, it may exhibit a convenient monotonic function along the interfacial region [24]. In this work, the subscript 1 will represent CO_2, 2 is for n-C_7H_{16} and 3 for C_7H_8.

In Eq. (15), $\Delta\Omega = \Omega + P^0$, where Ω is the grand thermodynamic potential, which is given by:

$$\Omega = a - \sum_{i=1}^{n_c} \rho_i \mu_i^0 \tag{16}$$

where a is the Helmholtz energy density of the homogeneous system (see Eq. 6), ρ_i and μ_i^0 have been described before.

Following the formalism of the SGT, ρ_i in Eqs. (15) and (16) are implicitly related by the following algebraic equation:

$$\sqrt{c_s}\left[\mu_k(\rho) - \mu_k^0\right] = \sqrt{c_k}\left[\mu_s(\rho) - \mu_s^0\right] \qquad i = 1, 2, s\text{-}1, s, s+1, \ldots, n_c \tag{17}$$

Form Eqs. (17) it is possible to calculate the interfacial molar concentration in the ρ*'s* projection. It is worth mentioning here that the ρ*'s* projection provides a route to evaluate the surface activity or absolute adsorption / desorption of species along the interface region. In the ρ*'s* projection, the geometrical condition $d\rho_i/d\rho_j = \infty$ denotes the accumulation of a species i at the interface region.

In summary, from Eqs. (16) to (18), it is possible to conclude that the determination of interfacial properties (interfacial molar concentration and interfacial tension) depends on the Helmholtz energy density of the homogeneous system (see Eq. 6), its derivatives on density (see Eqs. (15)), the bulk phase equilibrium boundaries, calculated from Eqs. (6) and (15), and the value of the pure influence parameter, c_i.

In the original SGT, c_i is defined as a constant, but modern versions of this theory reflect that this parameter should be a function of the direct correlation function of the homogeneous fluid. As this definition proves to be intractable from an analytical viewpoint, approximations have been used to calculate this parameter (see Ref. [73] for a complete description of c_i). The most common route to calculate the c_i value using an EoS was proposed by Carey [70,74]. In this approach, c_i is calculated at the boiling temperature from experimental γ values (γ_{exp}) and Eq. (16) applied for pure fluid as it follows:

$$c_i\left(T^0\right)=\gamma_{exp}^2\left(T^0\right)\left(\int_{\rho_i^V}^{\rho_i^L}\sqrt{2\left(a-\rho_i\mu_i^0+P^0\right)}d\rho_i\right)^{-2} \tag{18}$$

where the γ_{exp} data can been taken from the NIST REFPROP data base [49]. Recently, for the case of chain-like fluids modelled from the SGT and SAFT VR Mie EoS, c_i can be calculated from the following correlation: [73]

$$\sqrt{\frac{c_i}{N_{av}^2\varepsilon\sigma^5}}=m_{si}\left(0.12008+2.21979\alpha\right) \tag{19}$$

From Eqs. (18) and (19), it is possible to observe that c_i can be calculated by using the same molecular parameters (m_s, λ_r , λ_a, ε, σ, χ) than those used to describe the homogenous properties. In this work, the c_i value for CO_2 and C_7H_8 is calculated from Eq. (18) whereas Eq. (19) is used n-C_7H_{16}. The corresponding numerical values are summarized in Table 2.

4. Results and discussions

An integrated approach to simultaneously describe bulk phase densities for liquid and vapor phases and interfacial properties, including interfacial tensions and interfacial concentration in the interfacial zone is presented here. This approach combines experimental determinations and theoretical modeling and is applied for the case of CO_2 + {(1-*v*) n-C_7H_{16} + *v* C_7H_8}, with *v* = 0, 0.25, 0.50, 0.75, 1 at 344.15 K and over the pressure range 0.1 to 8 MPa.

On the basis of the classification of van Konynenburg and Scott [75], the binary CO_2 + C_7H_8 exhibits Type I phase behavior. *i.e.*, this binary mixture displays a continuum critical line connecting their pure components critical points. This critical line indicates that this type of mixture is characterized by a completely miscible liquid phase in every temperature / pressure condition. This fact implies that all subcritical states of this type exhibit only vapor – liquid equilibria (VLE). The binary CO_2 + n-C_7H_{16} is classified as Type II phase behavior, which exhibits a similar critical line than Type I plus a heteroazeotropic line. The heteroazeotropic line starts at low temperature-low pressure and ends in an upper critical end point (UCEP). This type of phase behavior states that the mixture exhibits both VLE and vapor – liquid – liquid equilibria (VLLE). For the case of the ternary mixture, it can be classified as a ternary Type II phase behavior following the phase diagrams proposed by Bluma and Dieters [76]. The ternary phase diagram for this type exhibits two binary subsystems Type I (CO_2 + C_7H_8 and C_7H_8 + n-

C_7H_{16}) and one binary subsystem of Type II (CO_2 + n-C_7H_{16}). The critical surfaces of this ternary system are characterized by a liquid – vapor critical surface, a liquid – liquid critical surface at low temperatures and a heteroazeotropic or three-phase region, which show UCEPs.

On the basis of the classification from Konynenburg and Scott [75] and Bluma and Dieters [76] and considering the available experimental data and theoretical predictions of the phase equilibria for this ternary mixture and its CO_2 binary sub-systems, it is possible to infer that the mixtures studied here will only display vapor – liquid equilibrium (VLE) at 344.15 K and over the pressure range (0.1 to 8) MPa. In the following section, we will present our experimental results and theoretical modeling for bulk mass densities, the interfacial tensions and finally, the interfacial concentrations for the CO_2 mixtures considered in this work.

4.1 Mass bulk densities for carbon dioxide + n-heptane + toluene mixtures

The bulk phase equilibria for this ternary system as a function of (P, T, x, y) have been recently measured and reviewed by Al Ghafri et al. [33]. In order to complement the available experiential data of bulk phase equilibria (P, T, x, y), this work is focused on the experimental measurements and theoretical modeling of bulk phase mass densities at vapor and liquid state at 344.15 K.

Tables 4 to 8 summarize the experimental determinations for the bulk mass densities for vapor ($\hat{\rho}_G$) and liquid ($\hat{\rho}_L$) phases at 344.15 K and over the pressure range 0.1 MPa to 8 MPa. These Tables include the experimental data for the ternary systems: CO_2 + {(1-v) n-C_7H_{16} + v C_7H_8}, with v = 0, 0.25, 0.50, 0.75, 1. Figure 1 shows the corresponding density phase diagram together with the predictions of the SAFT VR Mie EoS. Inspection of the Figure reveals that the mixture densities of CO_2 + {(1-v) n-C_7H_{16} + v C_7H_8}, behave ordinarily (*i.e.*, they do not exhibit barotropic inversion), and that the SAFT-VR-Mie model is reliable for predicting the phase equilibria up to 8 MPa. For a fixed pressure, the mass density increases as the liquid volume fraction of toluene (v) increases. From Figure 1, it is also possible to observe that at higher pressures (*i.e.*, when the mixture approaches its critical state), the theoretical predictions deviate from the experimental data. This deviation is more notorious at the vapor phase than the liquid phase due to the incompressibility of the liquid. This behavior is caused by the over-prediction of the critical pressure. However, this deficiency can be overcome by using a crossover methodology (see for instance Ref. [77,78]) or by rescaling the phase behavior predictions to the experimental value of the critical pressure. Table 9 summarizes the corresponding comparison between the experimental determinations and theoretical modeling expressing this as the absolute average deviation (AAD) in both liquid and vapor mass density for the systems investigated here. From this Table, it is possible to observe

that the maximum $AAD\rho$ are 1.56 % and 5.97 % for the liquid and vapor densities, respectively. Finally, it is not possible to compare the experimental data reported here to the previous experimental works because no experimental data have been reported before at the conditions explored here. However, some selected data from Medina-Bermúdez et al. [37] are close enough to make a comparison for the bulk liquid density in the CO_2 + n-C_7H_{16} binary mixture. In this case, the $AAD\rho$ was 0.44 %. A second possible comparison is the case of the bulk liquid density in the CO_2 + C_7H_8 binary mixture. For this binary system, Zirrahi et al. [42] has been reported the bulk liquid density as a function of temperature, pressure and mole fraction. Using an interpolation of that work at the appropriate conditions (344 K and 0.1-8 MPa), we are found an $AAD\rho$ = 0.14 %

4.2 Interfacial tensions for carbon dioxide + n-heptane + toluene mixtures

Interfacial tensions data for CO_2 + {(1-v) n-C_7H_{16} + v C_7H_8} systems have been previously reported for v = 0 in the temperature range 313.15 to 393.15 K and from 0.1 to 11.2 MPa [46,47,48]. In this work, Table 4 summarizes new experimental data for this mixture at 344.15 K. Interpolating the previous experimental works at 344.15 K, one finds that the interfacial tension data reported here are complementary and consistent with the previous ones. In fact, the absolute average deviation in interfacial tension ($AAD\ \gamma$) is lower than 2 %. For other values of v (*i.e.*, v = 0.25, 0.50, 0.75, 1), Tables 5 to 8 include the experimental determinations of interfacial tensions. Figure 2 displays the corresponding interfacial tensions together with the predictions of the SGT + SAFT VR Mie EoS. Inspection of this Figure reveals that the interfacial tensions for CO_2 + {(1-v) n-C_7H_{16} + v C_7H_8} mixtures behave as it is expected. In other words, for each value of v, the interfacial tension decreases as the pressure increase, and for a fixed pressure, the interfacial tension increases with v values. Table 9 summarizes the absolute average deviation (AAD) for the interfacial tension. Comparing the experimental data to the theoretical predictions, it is possible to conclude that SGT + SAFT VR Mie EoS approach overpredicts the experimental data of interfacial tension with maximum AADγ of 8.2 %. The observed over prediction in interfacial tension is caused by the inaccuracies of the EoS model near the critical state. In fact, this value reduces notoriously when only the experimental range is considered.

Finally, the theoretical accuracy obtained from the SGT + SAFT VR Mie EoS approach for the case of CO_2 + n-C_7H_{16} is similar than those reported by Niño Amézquita et al., [46] who used SGT + PCP-SAFT-EoS. However, these authors obtain better agreements near to the critical state due to the used route to obtained the molecular parameters.

4.3 Interfacial concentrations for carbon dioxide + n-heptane + toluene mixtures

Besides phase equilibrium, mass bulk densities and interfacial tensions, the theoretical approach provides a route to describe other interfacial properties such as the concentration profiles of species (ρ_i) at the interfacial zone. Figure 3 shows the concentration profiles for the case of CO_2 binary mixtures (*i.e.*, v = 0 and 1) at three pressure conditions (2, 6 and 8 MPa). From the $\rho_{CO2} - \rho_s$ projections, it is possible to observe that CO_2 always exhibits positive surface activity (as reflected in the Figure by the maximum observed for the concentration profile), whereas n-C_7H_{16} and C_7H_8 do not exhibit surface activity (monotonic behavior of its interfacial concentration). Figure 3 also reports the point of maximum interfacial concentration for CO_2 (*i.e.,* maximum surface activity) and clearly shows that the surface activity of CO_2 persists and increases with pressure. Based on the localization and magnitude of the maximum surface activity of CO_2, it is possible to note that CO_2 exhibits higher surface activity in n-C_7H_{16} than C_7H_8.

For the case of ternary systems (*i.e.*, v = 0.25; 0.50 and 0.75), Figure 4.a illustrates the $\rho_{CO2} - \rho_{C7H16} - \rho_{C7H8}$ projections at three pressure conditions (2, 6 and 8 MPa). For all cases, CO_2 always exhibits positive surface activity. Specifically, it is observed that for each ternary system, v = constant, the surface activity of CO_2 follows the same patterns than those observed for the case of binary systems (*i.e.*, its increases with pressure). For a fixed isobaric condition, the surface activity of CO_2 decreases as v increases, which is the expected behavior from the surface activity noted in the binary subsystems (v = 0 and 1). According to the interfacial profiles showed in Figure 4.a, it is possible to observe that C_7H_8 does not exhibit surface activity, whereas the n-C_7H_{16} does not exhibit surface activity at v = 0.25 and 0.50, but v = 0.75, n-C_7H_{16} displays surface activity at low pressure in a very narrow range, as it is shown in Figure 4.b.

5. Conclusions

In this work, bulk phase mass densities and interfacial tension of CO_2 + {(1-v) n-C_7H_{16} + v C_7H_8}, with v = (0; 0.25; 0.50; 0.75; 1) at 344.15 K and over the pressure range 0.1 to 8 MPa have been determined and theoretically modeled. Based on the experimental and modeling results, the bulk phase densities do not exhibit barotropic inversion and the model results adequate for describing the phase behavior with a maximum deviation of 1.6 % for the liquid phase and 6.0 % for the vapor phase. The SGT + SAFT VR Mie EoS model provides a reliable route for predicting the interfacial tension (showing an AADγ < 9 %) and interfacial concentration profiles, which reflects the selective adsorption of the component at the interfacial zone. For the mixtures considered here, it is possible to conclude that interfacial tension

decreases as the pressure or the percentage of toluene increase. Finally, CO_2 is always adsorbed along the interfacial zone, showing a surface activity that increases with pressure or the percentage of n-heptane. Toluene does not exhibit surface activity, whereas n-heptane only exhibits surface activity at $v = 0.75$ and in a low pressure in a very narrow range.

Finally, one can recognize that further refinements by the way of introducing new parameters and fitting constant could be carried out for the correlation of the bulk mass density and interfacial tension near to the critical state to reduce the absolute average deviation. However, as it was described in this work, the methodology applied here is based on the use of physically-sound parameters of pure components and binary mixtures that can be directly transferred to perform molecular simulations.

Funding sources

This work was financed by FONDECYT, Santiago, Chile (Project 1150656), and supported by the U.K. Engineering and Physical Sciences Research Council (EPSRC) through research grants to the Molecular Systems Engineering group (Grants EP/E016340, EP/I018212 and EP/J014958).

List of symbols

a_1	=	first-order perturbation terms of hard sphere
a_2	=	second-order perturbation terms of hard sphere
a_3	=	third-order perturbation terms of hard sphere
a	=	Helmholtz energy density
A	=	Helmholtz energy
c_i	=	influence parameter
C	=	constant for the Mie potential
d_e	=	equatorial diameter of the drop
d_i	=	hard-sphere diameter of fluid *i*
d_n	=	internal diameter of the needle
d_s	=	horizontal diameter of the drop
f	=	Laplace Capillary function
g	=	local gravitational constant
$g_{ii}^{Mie}(\sigma)$	=	radial distribution function of the Mie potential
k_B	=	Boltzmann's constant
k_{ij}	=	interaction parameter for the EoS mixing rule
m_{si}	=	molecular chain length (spherical segments) of component i
n_c	=	number of components
N	=	number of molecules
N_{av}	=	Avogadro's constant
P	=	absolute pressure
r_{ij}	=	center-center distance
T	=	absolute temperature
u_c	=	combined standard uncertainty
v	=	volume fraction for toluene in liquid state
V	=	volume
V_d	=	volume of the drop
x, y	=	mole fractions for liquid and vapor phases, respectively
Wo	=	dimensionless Worthing number

Greek

α	=	van der Waals' constant
β	=	$1 / (k_B T)$
χ	=	parameter in SAFT EoS
$\delta\Delta\rho$	=	standard uncertainty in density
δp	=	standard uncertainty in pressure
ε	=	potential well depth
ϕ^{Mie}	=	Mie potential
γ	=	interfacial tension
η_i	=	packing fraction of fluid *i*
Λ	=	thermal de Broglie´s wavelength
λ_a	=	attraction parameter of the intermolecular potential
λ_r	=	repulsion parameter of the intermolecular potential
μ	=	chemical potential
ρ	=	molar density
$\hat{\rho}$	=	mass density
σ	=	effective segment diameter
$\sigma(\gamma)$	=	standard deviation of γ
Ω	=	grand thermodynamic potential

Superscripts

CHARI	=	chain and ring contribution in SAFT - EoS
hs	=	Carnahan and Starling hard sphere
MONO	=	monomer contribution in SAFT - EoS
IG	=	ideal gas contribution in SAFT - EoS
V	=	vapor bulk phase
L	=	liquid bulk phase
0	=	equilibrium state

Subscripts

exp	=	experimental
i,j,k	=	components
L	=	liquid bulk phase
V	=	vapor bulk phase

Table 1 Gas chromatography (*GC*) purities (mass fraction), liquid mass densities ($\hat{\rho}$) and interfacial tensions (γ) of pure n-alkanes at 344.15 K and 101.3 kPa[a]

component (purity / mass fraction)	$\hat{\rho}$ (kg m^{-3})		γ (mN m^{-1})	
	Exp.	*Lit.*[b]	*Exp.*	*Lit.*[b]
carbon dioxide or CO_2 (0.999)	1.5630	1.5629	---	---
n-heptane or n-C_7H_{16} (0.999)	648.30	648.53	15.14	15.33
toluene or C_7H_8 (0.999)	828.22	828.27	22.38	22.39

[a] Measurement uncertainties are: $\hat{\rho} \pm 5 \times 10^{-3}$ kg m^{-3}; $\gamma \pm 0.01$ mN m^{-1}; $P \pm 0.10$ kPa; $T \pm 0.10$ K

[b] Experimental data have been taken from NIST – REFPROP data base [49].

Table 2. Thermophysical properties of the pure components[a,b]

Fluid	m_s	ε / k_B / K	σ / Å	λ_r	λ_a	$10^{20} \times c_i$ / (J m^5 mol^{-2})[c]
carbon dioxide (CO_2)	1	353.55	3.741	23.000	6.66	2.768
n-heptane (n-C_7H_{16})	2	436.13	4.766	23.807	6.00	49.137
toluene (C_7H_8)	3	268.24	3.685	11.796	6.00	31.020

[a] The molecular parameters of the SAFT VR Mie EoS have been taken from Avendaño et al. [63] for CO_2, from Mejía et al. [58] for n-C_7H_{16} and from Müller and Mejía [32] for C_7H_8 ; [b] $\chi = 0$ for CO_2 and n-C_7H_{16}; $\chi = 1.4938$ for C_7H_8. [c] c_i values have been calculated from Eq. (18) for CO_2 and C_7H_8 were the experimental γ data which have been taken from NIST-REFPROP data base [49]. For n-C_7H_{16}, it is calculated from Eq. (19)

Table 3. Binary parameters for mixing rules and statistic deviations in vapor pressure and vapor mole fraction for VLE correlations[a]

System	*T* / K	k_{ij}	***AADP %***	***% Δy₁***	*Ref.*
CO_2 + n-C_7H_{16}	343.15	0.060	2.24	0.24	[66]
CO_2 + C_7H_8	333.15	0.025	5.54	0.28	[67]
	352.15	0.040	3.66	0.45	[68]
	344.15	0.034	---	---	
n-C_7H_{16} + C_7H_8	348.15	-0.040	6.92	0.71	[69]

[a] statistic deviations: Absolute Average Deviation in pressure: $\%AADP = (100/N_p) \sum_{i=1,Np} |P_i^{cal}-P_i^{exp}| / P_i^{exp}$ and deviation in vapor mole fraction, $\% \Delta y_1 = (100/N_p) \sum_{i=1,Np} |y_i^{cal}-y_i^{exp}|$

Table 4 Experimental bulk phase mass densities and interfacial tensions for CO_2 + {(1-v) n-C_7H_{16} + v C_7H_8}, v = 0 at T = 344.15 K.[a]

P (MPa)	$\hat{\rho}_G$ (kg m^{-3})	$\hat{\rho}_L$ (kg m^{-3})	γ (mN m^{-1})
0.10	2.62	639.30	15.46
1.00	16.08	642.60	13.33
2.00	32.92	646.20	11.22
3.00	51.75	649.70	9.35
4.00	72.57	652.90	7.74
5.00	95.39	656.00	6.38
6.00	120.20	659.00	5.10
7.00	147.00	661.70	3.69
8.00	175.79	664.30	2.67

[a] Measurement uncertainties are: $\hat{\rho} \pm 5 \times 10^{-3}$ kg m^{-3}; $\gamma \pm 0.01$ mN m^{-1}; $P \pm 10^{-4}$ MPa; $T \pm 0.10$ K

Table 5 Experimental bulk phase mass densities and interfacial tensions for CO_2 + {(1-v) n-C_7H_{16} + v C_7H_8}, v = 0.25 at T = 344.15 K.[a]

P (MPa)	$\hat{\rho}_G$ (kg m^{-3})	$\hat{\rho}_L$ (kg m^{-3})	γ (mN m^{-1})
0.10	5.18	684.70	16.37
1.00	14.82	686.90	14.66
2.00	34.52	689.40	12.97
3.00	54.48	692.00	11.3
4.00	70.72	694.70	9.41
5.00	97.47	697.40	7.71
6.00	126.95	700.30	5.85
7.00	157.80	703.20	4.33
8.00	194.17	706.20	2.90

[a] Measurement uncertainties are: $\hat{\rho} \pm 5 \times 10^{-3}$ kg m^{-3}; $\gamma \pm 0.01$ mN m^{-1}; $P \pm 10^{-4}$ MPa; $T \pm 0.10$ K

Table 6 Experimental bulk phase mass densities and interfacial tensions for CO_2 + {(1-v) n-C_7H_{16} + v C_7H_8}, v = 0.50 at T = 344.15 K.[a]

P (MPa)	$\hat{\rho}_G$ (kg m^{-3})	$\hat{\rho}_L$ (kg m^{-3})	γ (mN m^{-1})
0.10	4.57	729.20	17.57
1.00	17.54	732.60	15.89
2.00	35.90	736.10	14.06
3.00	54.03	739.20	12.06
4.00	71.62	741.90	10.07
5.00	97.85	744.30	8.24
6.00	124.67	746.40	6.71
7.00	155.88	746.60	5.04
8.00	192.64	746.80	- - -

[a] Measurement uncertainties are: $\hat{\rho} \pm 5 \times 10^{-3}$ kg m^{-3}; $\gamma \pm 0.01$ mN m^{-1}; $P \pm 10^{-4}$ MPa; $T \pm 0.10$ K

Table 7 Experimental bulk phase mass densities and interfacial tensions for CO_2 + {(1-v) n-C_7H_{16} + v C_7H_8}, v = 0.75 at T = 344.15 K.[a]

P (MPa)	$\hat{\rho}_G$ (kg m^{-3})	$\hat{\rho}_L$ (kg m^{-3})	γ (mN m^{-1})
0.10	6.83	773.90	19.62
1.00	18.25	775.80	17.76
2.00	35.06	777.70	15.86
3.00	53.93	779.40	13.57
4.00	75.27	781.00	11.58
5.00	99.61	782.30	9.50
6.00	123.41	783.50	7.68
7.00	155.39	784.50	5.80
8.00	193.11	783.50	- - -

[a] Measurement uncertainties are: $\hat{\rho} \pm 5 \times 10^{-3}$ kg m^{-3}; $\gamma \pm 0.01$ mN m^{-1}; $P \pm 10^{-4}$ MPa; $T \pm 0.10$ K

Table 8 Experimental bulk phase mass densities and interfacial tensions for CO_2 + {(1-v) n-C_7H_{16} + v C_7H_8}, v = 1.00 at T = 344.15 K.[a]

P (MPa)	$\hat{\rho}_G$ (kg m^{-3})	$\hat{\rho}_L$ (kg m^{-3})	γ (mN m^{-1})
0.10	4.82	819.20	21.62
1.00	16.70	820.50	19.70
2.00	31.57	822.00	17.62
3.00	49.92	823.50	15.63
4.00	71.22	824.90	13.27
5.00	95.45	826.30	10.89
6.00	122.64	827.70	8.64
7.00	152.77	829.00	6.70
8.00	180.40	822.90	5.00

[a] Measurement uncertainties are: $\hat{\rho} \pm 5 \times 10^{-3}$ kg m^{-3}; $\gamma \pm 0.01$ mN m^{-1}; $P \pm 10^{-4}$ MPa; $T \pm 0.10$ K

Table 9 Absolute average deviation (AAD) in liquid and vapor densities and interfacial tension predictions for the systems CO_2 + {(1-v) n-C_7H_{16} + v C_7H_8} at 344.15 K [a]

	v = 0	v = 0.25	v = 0.50	v = 0.75	v = 1.00
% AAD $\hat{\rho}_G$	2.90	5.42	5.32	5.97	3.96
% AAD $\hat{\rho}_L$	1.56	0.50	0.38	0.07	0.21
% AAD γ	8.25	7.76	7.86	6.71	7.40

[a] Absolute Average Deviation: $\%AAD\delta = (100/N_p) \sum_{i=1,Np} |\delta_i^{cal}-\delta_i^{exp}| / \delta_i^{exp}$ ($\delta = \rho$ or γ)

Figure Captions

[1] Pressure (*P)* vs. bulk mass density ($\hat{\rho}$) diagram for CO_2 + {(1-*v*) n-C_7H_{16} + *v* C_7H_8} at 344.15 K. (—) predicted from SAFT-VR-Mie EoS with k_{ij} reported in Table 3. Experimental data: (●) *v* = 0.00; (○) *v* = 0.25; (□) *v* = 0.50; (◇) *v* = 0.75; (■) *v* = 1.00;

[2] Interfacial tension (γ) as a function of pressure (*P)* for CO_2 + {(1-*v*) n-C_7H_{16} + *v* C_7H_8} at 344.15 K. (—) predicted from SGT + SAFT-VR-Mie EoS with $c_i s$ reported in Table 2 and k_{ij} reported in Table 3. Experimental data: (●) *v* = 0.00; (○) *v* = 0.25; (□) *v* = 0.50; (◇) *v* = 0.75; (■) *v* = 1.00.

[3] Concentration profiles in the $\rho_{CO2} - \rho_s$ projection at three pressures for CO_2 + {(1-*v*) n-C_7H_{16} + *v* C_7H_8} mixtures at 344.15 K. Prediction from SGT + SAFT-VR-Mie –EoS with with $c_i s$ reported in Table 2 and k_{ij} reported in Table 3. (—) *v* = 0.00 (*s* = n-C_7H_{16}); (– –) *v* = 1.00 (*s* = C_7H_8);. (●) bulk phase equilibrium densities, (○) maximum CO_2 surface activity.

[4.a] Concentration profiles in the $\rho_{CO2} - \rho_{C7H8} - \rho_{C7H16}$ projection at three pressures for CO_2 + {(1-*v*) n-C_7H_{16} + *v* C_7H_8} mixtures at 344.15 K. Prediction from SGT + SAFT-VR-Mie –EoS with with c_i, c_j reported in Table 2 and k_{ij} reported in Table 3. (—) *v* = 0.25; (– –) *v* = 0.50; (— – – —) *v* = 0.75; (●) bulk phase equilibrium densities, (○) maximum CO_2 surface activity. (□) maximum n-C_7H_{16} surface activity.

[4.b] Zoom of Fig. [4.a] Concentration profiles in the $\rho_{CO2} - \rho_{C7H8} - \rho_{C7H16}$ projection at three pressures for CO_2 + {(1-*v*) n-C_7H_{16} + *v* C_7H_8} mixtures at 344.15 K. Prediction from SGT + SAFT-VR-Mie –EoS with with $c_i s$ reported in Table 2 and k_{ij} reported in Table 3. (— – – —) *v* = 0.75; (●) bulk phase equilibrium densities, (○) maximum CO_2 surface activity. (□) maximum n-C_7H_{16} surface activity.

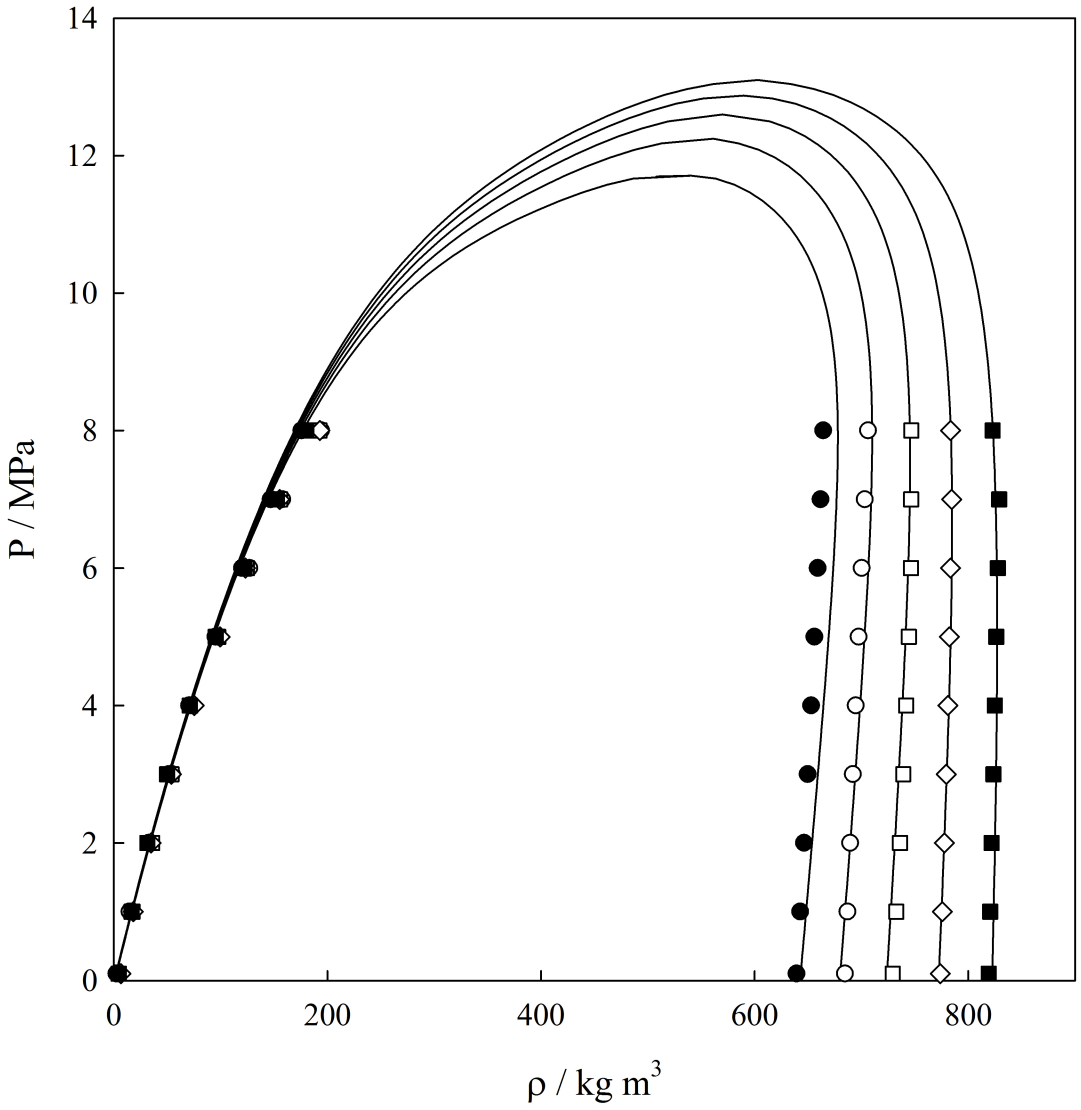

Figure 1

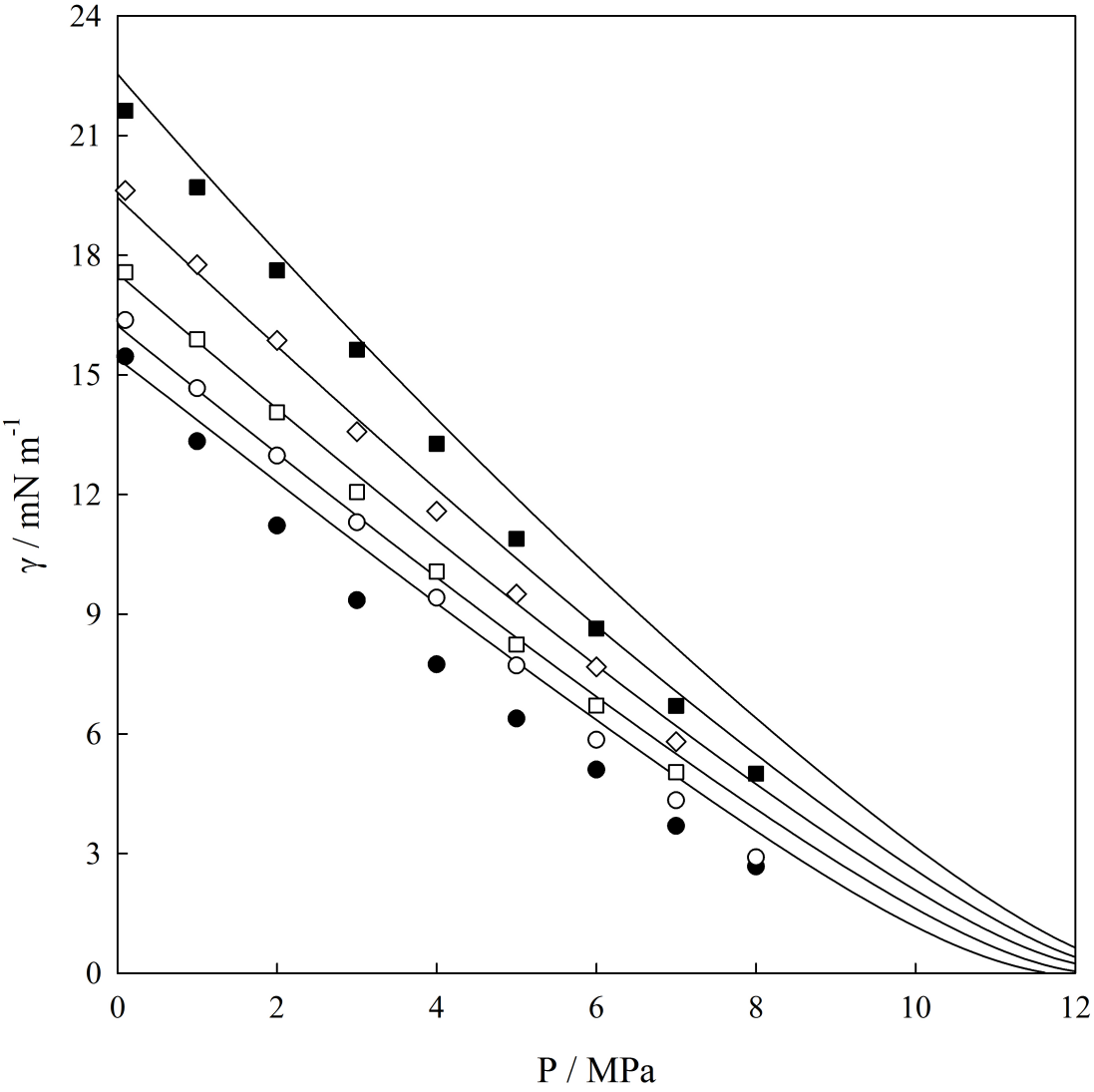

Figure 2

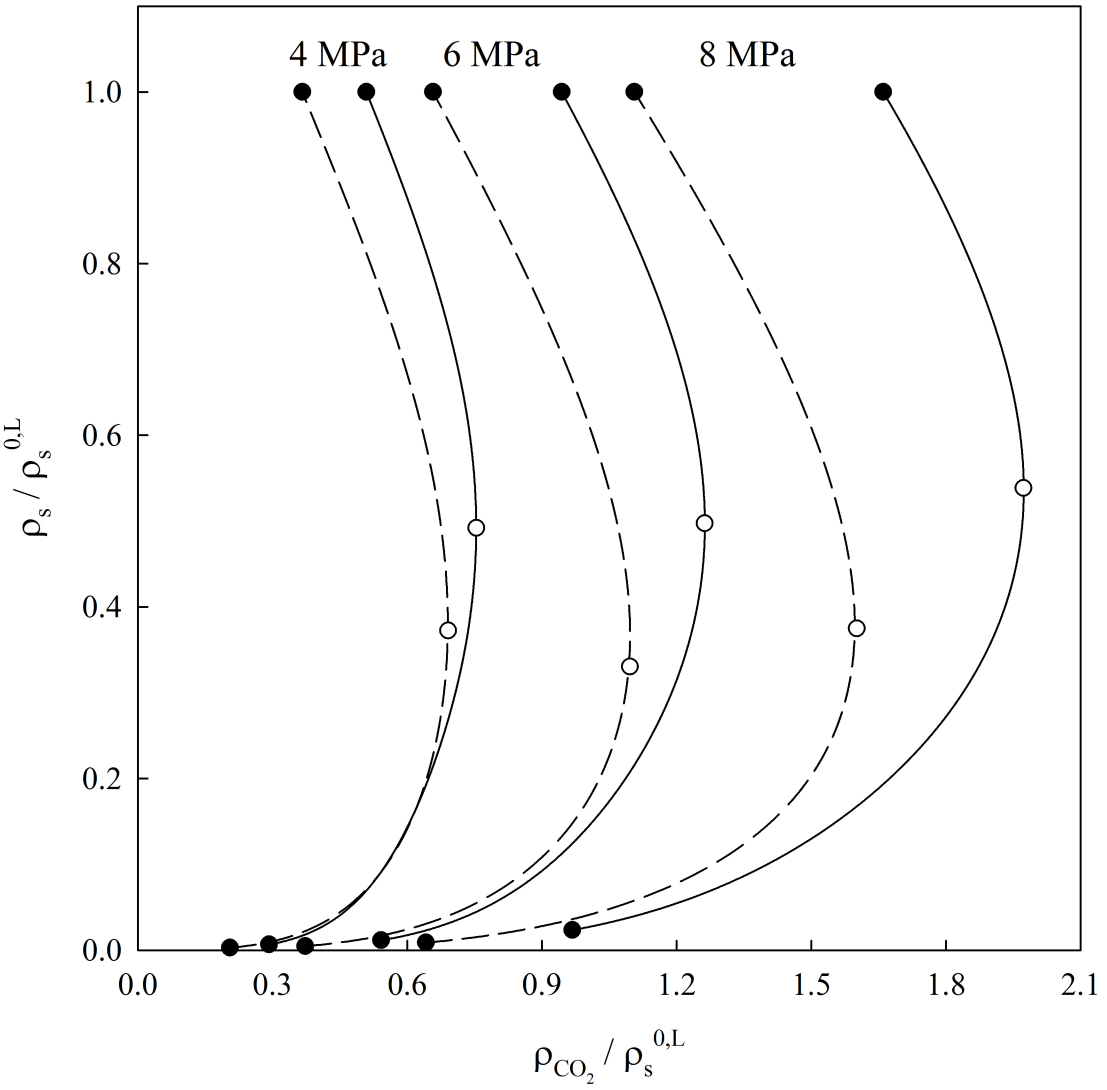
4 MPa
6 MPa
8 MPa
1.0
0.8
0.6
0.4
0.2
0.0
0.0
0.3
0.6
0.9
1.2
1.5
1.8
2.1
ρs / ρs 0,L
ρCO2 / ρs 0,L

Figure 3

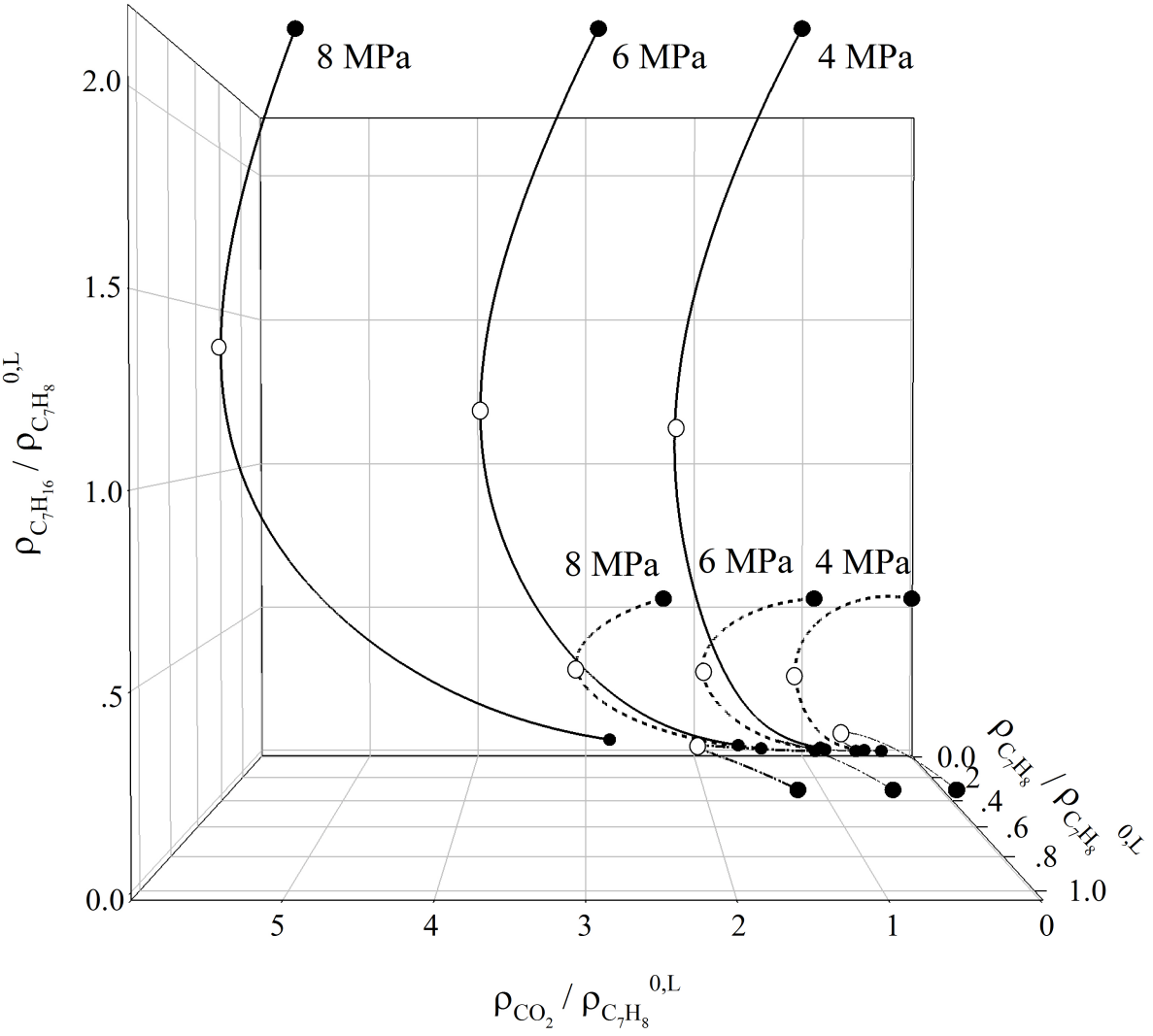
8 MPa
6 MPa
4 MPa
8 MPa
6 MPa
4 MPa
2.0
1.5
1.0
.5
0.0
$\rho_{C_7H_{16}} / \rho_{C_7H_8}^{0,L}$
5
4
3
2
1
0
$\rho_{CO_2} / \rho_{C_7H_8}^{0,L}$
0.0
.2
.4
.6
.8
1.0
$\rho_{C_7H_8} / \rho_{C_7H_8}^{0,L}$

Figure 4.a

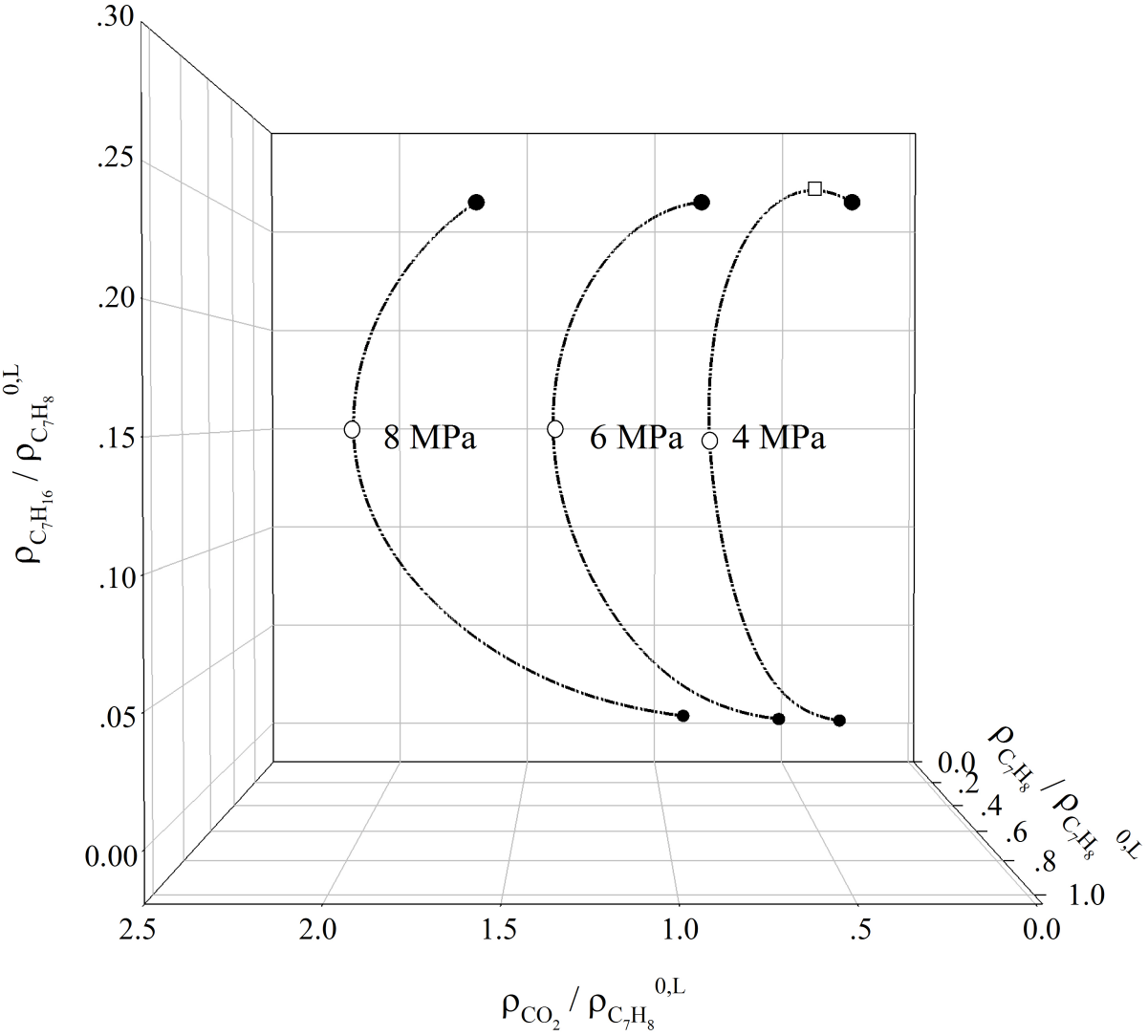
.30
.25
.20
.15
.10
.05
0.00
$\rho_{C_7H_{16}} / \rho_{C_7H_8}^{0,L}$
8 MPa
6 MPa
4 MPa
2.5
2.0
1.5
1.0
.5
0.0
$\rho_{CO_2} / \rho_{C_7H_8}^{0,L}$
0.0
.2
.4
.6
.8
1.0
$\rho_{C_7H_8} / \rho_{C_7H_8}^{0,L}$

Figure 4.b

References

[1] Hemmati-Sarapardeh A, Ayatollahi S, Ghazanfari MH, Masihi, M. Experimental determination of interfacial tension and miscibility of the CO_2-crude oil system; temperature, pressure, and composition effects. J. Chem. Eng. Data 2014;59:61–9.

[2] Zolghadr A, Escrochi M, Ayatollahi S. Temperature and composition effect on CO_2 miscibility by interfacial tension measurement. J. Chem. Eng. Data 2013;58:1168–75.

[3] Alvarado V, Manrique E. Enhanced Oil Recovery: An update Review. Energies 2010;3:1529–75.

[4] Mahdavi E, Zebarjad FS, Taghikhani V, Ayatollahi S. Effects of paraffinic group on interfacial tension behavior of CO_2 − asphaltenic crude oil systems. J. Chem. Eng. Data 2014;59:2563-69.

[5] Pedersen KS, Christensen PL, Shaikh, Phase behavior of petroleum reservoir fluids, 2ed. CRC Press, Boca Raton, 2014.

[6] Danesh A. PVT and Phase Behaviour of Petroleum Reservoir Fluids; Elsevier: Amsterdam, 2012.

[7] Chalbaud C, Robin M, Lombard JM, Martina F, Egermann P, Bertin H. Interfacial tension measurements and wettability evaluation for geological CO_2 storage. Adv. Water Resour. 2009;32:98–109.

[8] Verdier S, Carrier H, Andersen SI, Daridon JL. Study of pressure and temperature effects on Asphaltene stability in presence of CO_2. Energy Fuels 2006;20:1584–90.

[9] Orr FM, Heller JP, Taber J. Carbon dioxide flooding for enhanced oil recovery: Promise and problems. J. Am. Oil Chem. Soc. 1982;59:A810–17.

[10] Coutinho JAP, Jorgensen M, Stenby EH. Predictions of three-phase regions in CO_2-oil mixtures. J. Petrol. Sci. Eng. 1995;12:201–8.

[11] Gaspar Ravagnani ATFS, Ligero EL, Suslick SB. CO_2 sequestration through enhanced oil recovery in a mature oil field. J. Petrol. Sci. Eng. 2009;65:129–38.

[12] Cismondi M, Mollerup JM, Zabaloy MS. Equation of state modeling of the phase equilibria of asymmetric CO_2 + n-alkane binary systems using mixing rules cubic with respect to mole fraction. J. Supercrit Fluid. 2010;55:671–81.

[13] Flores M, Tardón M, Bidart C, Mejía A, Segura H. A topological approach to mass barotropic phenomena in asymmetric mixtures. Fluid Phase Equilib. 2012;313:171–81.

[14] Cismondi M, Rodríguez-Reartes SB, Milanesio JM, Zabaloy MS. Phase Equilibria of CO_2 + n-alkane binary systems in wide ranges of conditions: Development of predictive correlations based on cubic mixing rules. Ind. Eng. Chem. Res. 2012;51:6232–50.

[15] Georgiadis A. Interfacial Tension of Aqueous and Hydrocarbon Systems in the Presence of Carbon Dioxide at Elevated Pressures and Temperatures, Ph. D. Thesis, Imperial College London, 2011.

[16] Mejía A, Cartes M, Segura H, Müller EA. Use of equations of state and coarse grained simulations to complement experiments: describing the interfacial properties of carbon dioxide + decane and carbon dioxide + eicosane mixtures, J. Chem. Eng. Data 2014;59:2928–41.

[17] Cumicheo C, Cartes M, Segura H, Müller EA, Mejía A. High-pressure densities and interfacial tensions of binary systems containing carbon dioxide + n-alkanes: (n-dodecane, n-tridecane , n-tetradecane). Fluid Phase Equilibria 2014;380:82–92.

[18] Georgiadis A, Llovell F, Bismarck A, Blas FJ, Galindo A, Maitland GC, Trusler JPM, Jackson G. Interfacial tension measurements and modelling of (carbon dioxide + n-alkane) and (carbon dioxide + water) binary mixtures at elevated pressures and temperatures. J. Supercrit. Fluid 2010;55:743–54.

[19] Llovell F, Mac Dowell, N, Blas FJ, Galindo A, Jackson, G. Application of the SAFT-VR density functional theory to the prediction of the interfacial properties of mixtures of relevance to reservoir engineering. Fluid Phase Equilib. 2012;336: 137–50.

[20] Mejía A, Polishuk I, Segura H, Wisniak J. Estimation of interfacial behavior using the global phase diagram approach: I. Carbon dioxide–n-alkanes. Thermochim. Acta 2004; 411:171–76.

[21] Mejía A, Segura H, Wisniak J, Polishuk I, Correlation and prediction of interface tension for fluid mixtures. An approach based on cubic equations of state with the Wong-Sandler mixing rule. J. Phase Equilib. Diff. 2005;26:215–24.

[22] Müller EA, Mejía A. Interfacial properties of selected binary mixtures containing n-alkanes. Fluid Phase Equilib. 2009;282:68–81.

[23] Miqueu C, Mendiboure B, Graciaa C, Lachaise J. Petroleum mixtures: An efficient predictive method for surface tension estimations at reservoir conditions. Fuel 2008;87:612–21.

[24] Miqueu C, Mendiboure B, Graciaa C, Lachaise J. Modelling of the surface tension of binary and ternary mixtures with the gradient theory of fluid interfaces. Fluid Phase Equilib. 2004;218:189–203.

[25] Miqueu C, Mendiboure B, Graciaa C, Lachaise J. Modeling of the surface tension of multicomponent mixtures with the gradient theory of fluid interfaces. Ind. Eng. Chem. Res. 2005;44:3321–29.

[26] Fu D, Wei Y. Investigation of vapor-liquid surface tension for carbon dioxide and hydrocarbon mixtures by perturbed-chain Statistical associating fluid theory combined with density-gradient theory. Ind. Eng. Chem. Res. 2008;47:4490–95.

[27] Niño Amézquita OG, Enders S, Jaeger PT, Eggers R. Interfacial properties of mixtures containing supercritical gases. J. Supercrit Fluid 2010;55:724–34.

[28] Vilaseca O, Vega LF. Direct calculation of interfacial properties of fluids close to the critical region by a molecular-based equation of state. Fluid Phase Equilib. 2011;306:4–14

[29] Cárdenas H, Mejía A. Phase behaviour and interfacial properties of ternary system CO_2+ n-butane + n-decane: coarse-grained theoretical modelling and molecular simulations. Mol. Phys. 2016;114:2627–40.

[30] Neyt JC, Wender A, Lachet V, Malfreyt P. Modeling the pressure dependence of acid gas + n-alkane interfacial tensions using atomistic monte carlo simulations. J. Phys. Chem. C 2012;116:10563−72.

[31] Lafitte T, Apostolakou A, Avendaño C, Galindo A, Adjiman CS, Müller EA, Jackson G. Accurate statistical associating fluid theory for chain molecules formed from Mie segments. J. Chem. Phys. 2013;139:1545041–37.

[32] Müller EA, Mejía A. Extension of the SAFT-VR Mie EoS to model homonuclear rings and its parameterization based on the principle of corresponding states. Langmuir 2007;33:11518–29 (2017).

[33] Al Ghafri SZS, Maitland GC, Trusler JPM, Phase behavior of the system (Carbon Dioxide + n-Heptane + Methylbenzene): A Comparison between experimental Data and SAFT-γ-Mie Predictions. J. Chem. Eng. Data 2017; 62: 2826–36.

[34] Papaioannou V, Lafitte T, Avendaño C, Adjiman CS, Jackson G, Müller EA, Galindo A. Group contribution methodology based on the statistical associating fluid theory for heteronuclear molecules formed from Mie segments. J. Chem. Phys. 2014;140:054107.

[35] DECHEMA Gesellschaft für Chemische Technik und Biotechnologie e.V., Frankfurt am Main, Germany. https://cdsdt.dl.ac.uk/ detherm/, (retrieved February , 2018).

[36] Fenghour A, Trusler JPM, Wakeham WA. Densities and bubble points of binary mixtures of carbon dioxide and n-heptane and ternary mixtures of n-butane, n-heptane and n-hexadecane. Fluid Phase Equilib. 2001;185:349−58.

[37] Medina-Bermúdez M, Saavedra-Molina LA, Escamilla-Tiburcio W, Galicia-Luna LA, Elizalde-Solis O. (p, ρ, T) behavior for the binary mixtures carbon dioxide + heptane and carbon dioxide + tridecane. J. Chem. Eng. Data 2013;58:1255−64.

[38] Zhang X, Zhang X, Han B, Shi L, Li H, Yang G. Determination of constant volume heat capacity of mixed supercritical fluids and study on the intermolecular interaction. J. Supercrit. Fluids. 2002;24:193−201.

[39] Kalra H, Kubota H, Robinson DB, Ng HJ. Equilibrium phase properties of the carbon dioxide - n-heptane system. J. Chem. Eng. Data. 1978;23:317−21.

[40] Park SD, Kim CH, Choi CS. Phase equilibria and mixture densities measurements of carbon dioxide - toluene system under high pressure. Hwahak Konghak. 1990;28: 438−43.

[41] Poehler H, Kiran E, Volumetric properties of carbon dioxide + toluene at high pressures J. Chem. Eng. Data. 1996;41:482−86.

[42] Zirrahi M, Azinfar B, Hassanzadeh H, Abedi J. Measuring and modeling the solubility and density for CO_2 Toluene and C_2H_6 toluene systems. J. Chem. Eng. Data 2015;60:1592–99.

[43] Wu J, Pan Q, Rempel GL. Pressure-density-temperature behavior of CO_2 - acetone, CO_2 - toluene, and CO_2 - monochlorobenzene mixtures in the near-critical region. J. Chem. Eng. Data. 2004; 49:976−79.

[44] Sengers JMHL, Deiters UK, Klask U, Swidersky P, Schneider GM. Application of the Taylor dispersion method in supercritical fluids. Int. J. Thermophys. 1993;14:893−922.

[45] Wohlfarth Ch, Wohlfarth B. Numerical Data and Functional Relationships in Science and Technology, Vol. 16. Surface Tension of Pure Liquids and Binary Liquid Mixtures, Eds. Lechner, M. D. in Landolt-Börnstein, New Series Group IV Physical Chemistry; Springer Verlag Berlin: Heidelberg, 1997

[46] Niño Amézquita OG, Enders S, Jaeger PT, Eggers R. Interfacial properties of mixtures containing supercritical gases. J. Supercrit. Fluids. 2010;55:724−34.

[47] Jaeger PT, Alotaibi MB, Nasr-El-Din HA. Influence of compressed carbon dioxide on the capillarity of the gas-crude oil-reservoir water System. J. Chem. Eng. Data 2010;55:5246−51.

[48] Zolghadr A, Escrochi M, Ayatollahi S. Temperature and composition effect on CO_2 miscibility by interfacial tension measurement, J. Chem. Eng. Data 2013;58:1168−75.

[49] Lemmon EW, Huber ML, McLinden MO, NIST Standard reference database 23: Reference Fluid Thermodynamic and Transport Properties-REFPROP, Version 9.1, 2013.

[50] Hansen FK, A program system for interfacial tension and contact angle measurements by image analysis, Advanced Edition, Ramé-Hart instrument Co. USA, 2005

[51] Andreas JM, Hauser EA, Tucker WB, Boundary tension by pendant drops, J. Phys. Chem.1938; 42:1001–19.

[52] Taylor BN, Kuyatt CE, Guidelines for evaluating and expressing the uncertainty of NIST measurement results; NIST: Gaithersburg, MD, 1994.

[53] Berry JD, Neeson MJ, Dagastine RR, Chan DYC, Tabor RF. Measurement of surface and interfacial tension using pendant drop tensiometry. J. Colloid Interface Sci. 2015;454:226–37.

[54] Rusanov AI, Prokhorov VA. Interfacial Tensiometry, Elsevier, Amsterdam, 1996.

[55] Ambwani DS, Fort JrT. in: Good RJ, Stromberg RR. Pendant drop technique for measuring liquid boundary tensions. vol. 11, Plenum Press, New York, 1979.

[56] Evans MJB. in: Weir RD, de Loos ThW (Eds.), Measurement of surface and interfacial tension, in measurement of the thermodynamic properties of multiple phases, vol. VII, Elsevier, Amsterdam, 2006.

[57] Mie G. Zur kinetischen Theorie der einatomigen Körper. Ann. Phys. 1903; 316:657−97.

[58] Mejía A, Herdes C, Müller EA. Force fields for coarse-grained molecular simulations from a corresponding states correlation. Ind. Eng. Chem. Res. 2014;53:4131–41.

[59] Ramrattan NS, Avendaño C, Müller EA, Galindo AA corresponding-states framework for the description of the Mie family of intermolecular potentials. Mol. Phys. 2015;113:932–47.

[60] Gil-Villegas A, Galindo A, Whitehead PJ, Mills SJ, Jackson G, Burgess AN. Statistical associating fluid theory for chain molecules with attractive potentials of variable range. J Chem Phys. 1997;106:4168–86.

[61] London F. The general theory of molecular forces. Trans. Faraday Soc., 1937;33:8–26.

[62] Ervik Å, Mejía A, Müller EA. A web app providing SAFT-γ Mie force field parameters for thousands of molecular fluids. J. Chem. Inf. Model. 2016;56:1609–14. (http://bottledsaft.org)

[63] Avendaño C, Lafitte T, Galindo A, Adjiman CS, Jackson G, Müller EA. SAFT-γ force field for the simulation of molecular fluids. 1. A single-site coarse grained model of carbon dioxide. J. Phys. Chem. B 2011;115:11154–69.

[64] Müller EA, Jackson G. Force-Field Parameters from the SAFT-γ Equation of State for Use in Coarse-Grained Molecular Simulations. Annu. Rev. Chem. Biomol. Eng. 2014;5:405–27.

[65] Modell M, Tester J. Thermodynamics and its Applications, 3th ed., Prentice-Hall, New York, 1996

[66] Sako T, Sugeta T, Nakazawa N, Otake K, Sato M, Ishihara K, Kato M. High pressure vapor-liquid and vapor-liquid-liquid equilibria for systems containing supercritical carbon dioxide, water and furfural. Fluid Phase Equilib. 1995;108:293–303.

[67] Chen LB, Fang XG. Phase equilibria and CO_2 distribution in the CO_2 - Epoxide - Toluene systems. J. Nat. Gas Chem. 1994;3:255–66.

[68] Muhlbauer AL, Raal JD. Measurement and thermodynamic interpretation of high-pressure vapor-liquid equilibria in the toluene - CO_2 system. Fluid Phase Equilib. 1991;64:213–36.

[69] Liu Y, Xie R, Fan Z, Zan J. Isothermal vapor-liquid equilibrium for n-heptane and methylbenzene. Huaxue Gongcheng 1983;6:42-50,63.

[70] Carey BS. The Gradient Theory of Fluid Interfaces. Ph.D. Thesis, University of Minnesota, 1979.

[71] Carey BS, Scriven LE, Davis HT. Semiempirical theory of surface tension of binary systems. AIChE J. 1980;26:705-11.

[72] Mejía A, Segura H, Vega LF, Wisniak J. Simultaneous prediction of interfacial tension and phase equilibria in binary mixtures. An approach based on cubic equations of state with improved mixing rules. Fluid Phase Equilib. 2005;227:225–38.

[73] Garrido JM, Mejía A, Piñeiro MM, Blas FJ, Müller EA. Interfacial tensions of industrial fluids from a molecular-based square gradient theory. AIChE J. 2016;62:1781–94.

[74] Carey BS, Scriven LE, Davis HT. Semiempirical theory of surface tensions of pure normal alkanes and alcohols. AIChE J. 1978;24:1076–80.

[75] van Konynenburg P, Scott RL. Critical lines and phase equilibria in binary van der Waals mixtures. Philos. Trans. R. Soc. London 1980;298 A:495−540.

[76] Bluma M, Deiters UK. A classification of phase diagrams of ternary fluid systems. Phys. Chem. Chem. Phys. 1999;1:4307−13.

[77] Sun L, Zhao H, Kiselev SB, McCabe C. Predicting mixture phase equilibria and critical behavior using the SAFT-VRX approach. J. Phys. Chem. B 2005;109:9047–58.

[78] Sun L, Zhao H, Kiselev SB, McCabe C. Application of SAFT–VRX to binary phase behaviour: alkanes. Fluid Phase Equilib. 2005;228–229:275–82.